

## Article

# Fabrication of TaON/CdS Heterostructures for Enhanced Photocatalytic Hydrogen Evolution under Visible Light Irradiation

Fu Chen <sup>1,2</sup>, Haitao Fu <sup>1,2,\*</sup> , Xiaohong Yang <sup>2,\*</sup> , Shixian Xiong <sup>3</sup>  and Xizhong An <sup>2</sup> 

<sup>1</sup> Key Laboratory for Ecological Metallurgy of Multimetallurgical Mineral, Ministry of Education, Northeastern University, Shenyang 110819, China

<sup>2</sup> School of Metallurgy, Northeastern University, Shenyang 110819, China

<sup>3</sup> Jiangxi Provincial Key Laboratory for Simulation and Modelling of Particulate System, Jiangxi University of Science and Technology, Nanchang 330013, China

\* Correspondence: fuht@smm.neu.edu.cn (H.F.); yangxh@smm.neu.edu.cn (X.Y.)

**Abstract:** Developing high-performance photocatalysts for H<sub>2</sub> production via fabricating heterojunctions has attracted much attention. Herein, we design a simple strategy to prepare composites that consist of TaON/CdS hybrids via a hydrothermal process. The results show that the pristine CdS nanoparticles loaded with 20 wt% TaON (TC4) could maximize the photocatalytic hydrogen evolution rate to 19.29 mmol g<sup>-1</sup> h<sup>-1</sup> under visible light irradiation, which was 2.13 times higher than that of the pristine CdS (9.03 mmol g<sup>-1</sup> h<sup>-1</sup>) under the same conditions. The apparent quantum yield (AQY) of the TC4 nanocomposites at 420 nm was calculated to be 18.23%. The outstanding photocatalytic performance of the composites can be ascribed to the formation of heterojunctions. The electrochemical measurements indicate that the decoration facilitates the generation of extra photo-electrons, prolonging the recombination rate of photogenerated charge carriers, offering adequate active sites and improving catalytic stability. This study sheds light on the construction strategy and the deep understanding of the novel CdS-based composites for high-performance photocatalytic H<sub>2</sub> production.

**Keywords:** photocatalysts; TaON/CdS composites; hydrogen evolution; visible light irradiation



**Citation:** Chen, F.; Fu, H.; Yang, X.; Xiong, S.; An, X. Fabrication of TaON/CdS Heterostructures for Enhanced Photocatalytic Hydrogen Evolution under Visible Light Irradiation. *Catalysts* **2022**, *12*, 1110. <https://doi.org/10.3390/catal12101110>

Academic Editor: Rufino M. Navarro Yerga

Received: 31 August 2022

Accepted: 19 September 2022

Published: 25 September 2022

**Publisher's Note:** MDPI stays neutral with regard to jurisdictional claims in published maps and institutional affiliations.



**Copyright:** © 2022 by the authors. Licensee MDPI, Basel, Switzerland. This article is an open access article distributed under the terms and conditions of the Creative Commons Attribution (CC BY) license (<https://creativecommons.org/licenses/by/4.0/>).

## 1. Introduction

Since the discovery of photocatalytic water splitting on TiO<sub>2</sub> electrodes by Fujishima and Honda in 1972 [1], solar-driven hydrogen evolution from water splitting has become a promising method to solve the depletion of fossil fuels [2]. However, the quick recombination of the photogenerated charge carriers still limits the practical application of photocatalysts [3]. Obtaining highly efficient and stable photocatalysts is the key to improve the performance of the photocatalytic reactions [4]. Generally speaking, high-performance photocatalysts should possess a narrow bandgap [5], strong visible absorption [6], appropriate energy band position [7], good photocatalytic stability and abundant active sites for photocatalytic hydrogen evolution [8].

Attractive materials suitable for forming heterojunctions, such as sulfides [9], nitrides [10], and oxides [11,12], have been intensively studied. Among these materials, cadmium sulfide (CdS) renders excellent photocatalytic H<sub>2</sub> production performance, owing to the narrow energy bandgap (2.4 eV) and suitable conduction/valence band potential for hydrogen reductions [13]. However, the pristine CdS nanoparticles always suffer from fast charge recombination rates. Therefore, the methods that include heterojunction construction [14,15] and element doping [16] are applied to enhance the photocatalytic efficiency. Forming heterojunctions by loading co-catalysts has several advantages, such as facilitating the generation and transportation of photoinduced charge carriers [17], reducing the

electron–hole recombination [18], improving the photocatalytic activity of catalysts [19] and enhancing light harvesting ability [20]. However, the majority of studies focus on the decoration of MoS<sub>2</sub> due to its unique layer structure, proper bandgap (1.9 eV) and redox potentials, as well as its stable chemical properties [21]. One good example has been reported by Han et al., who demonstrated that MoS<sub>2</sub>/CdS heterostructures could efficiently retard the charge carrier recombination [22]. However, decoration with other guest materials needs to be further developed.

Tantalum oxynitride (TaON) has been proposed as a promising photocatalytic material for H<sub>2</sub> evolution, since its theoretical optical and electronic properties have been predicted to be suitable for photocatalytic H<sub>2</sub> evolution by density functional theory [23]. Compared to Ta<sub>2</sub>O<sub>5</sub> and Ta<sub>3</sub>N<sub>5</sub>, the appropriate band gap position [24] and good sunlight harvesting ability [25] make TaON an ideal candidate for photocatalytic water splitting under visible light irradiation. However, previous studies indicated that the photocatalytic hydrogen evolution efficiency of pristine TaON was limited by its ultrahigh charge recombination rate [26], poor photo-stability [27] and low quantum efficiency [28]. Therefore, it is necessary to stabilize and boost the photocatalytic performance of TaON by forming heterojunctions with other photocatalysts.

In this study, we prepared TaON-decorated CdS nanocomposites via the hydrothermal process of high-performance photocatalytic hydrogen production under visible light irradiation, which is rarely reported in the literature. The optimized ratios of TaON to CdS were determined by evaluating the photocatalytic H<sub>2</sub> evolution performances. The obtained photocatalysts achieved high quantum efficiency and excellent cycle stability. The mechanism of H<sub>2</sub> production performance after the formation of heterojunctions was studied with the aid of electrochemical experiments. This work provides a new way to prepare stable and high-performance photocatalysts for efficient hydrogen evolution.

## 2. Experimental

### 2.1. Materials

The chemicals used in this work were purchased from Sinopharm Chemical Reagent Co., Ltd. (Shanghai, China), including cadmium acetate (Cd(Ac)<sub>2</sub>·2H<sub>2</sub>O, 98%), thiourea (NH<sub>2</sub>CSNH<sub>2</sub>, 99%), tantalum oxide (Ta<sub>2</sub>O<sub>5</sub>, 99.99%), lactic acid (85%), and ethanol (99.5%). All of the reagents are directly used without further purification. All solutions were prepared with ultrapure water.

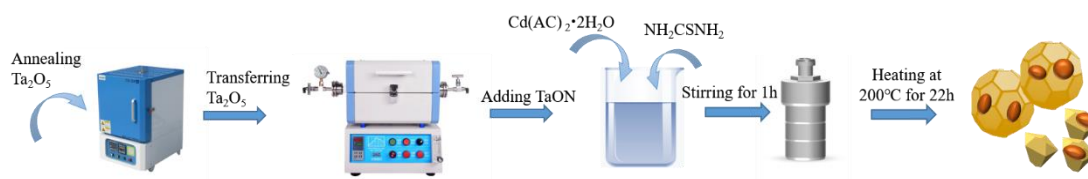
### 2.2. The Preparation of TaON Particles

TaON particles were prepared by a nitrogenization method. The commercial Ta<sub>2</sub>O<sub>5</sub> powders were placed in a ceramic boat and then transferred into a quartz tube furnace. The nitrogenization was achieved by heating the powders at 900 °C for 5 h, under an NH<sub>3</sub> gas flow of 20 mL·min<sup>-1</sup>. To avoid reoxidation, the NH<sub>3</sub> gas continued to flow through the powders during the cooling process.

### 2.3. The Preparation of TaON/CdS Nanocomposites

In a typical procedure, 0.3198 mg Cd (Ac)<sub>2</sub>·2H<sub>2</sub>O and 0.9134 mg thiourea were dissolved into 60 mL DI water with strong stirring for 2 h. The as-prepared TaON particles were then added to the above solution. After we continued stirring for another 2 h, this suspension was transferred to a 100-mL Teflon-lined stainless autoclave and heated at 200 °C for 22 h. The autoclave was allowed to be naturally cooled to room temperature. Afterwards, the samples were washed with ultrapure water and ethanol several times, followed by being dried at 60 °C for 12 h. Scheme 1 illustrates the preparation of the TaON/CdS composites. To obtain different loading amounts of TaON, the mass ratios of TaON to CdS were designed as 5, 10, 15, 20, 25 and 30 wt%, which was equal to the weight ratios of 1:20, 2:20, 3:20, 4:20, 5:20, 6:20, respectively. The obtained samples were labelled as TC1, TC2, TC3, TC4, TC5, TC6, TaON, and CdS. The elemental composition was measured by ICP-AES (inductively coupled plasma-atom emission spectrometry). The

results are listed in Table S1 in the supporting information, indicating that the molar ratios of TaON/CdS are consistent with the theoretical value.



**Scheme 1.** Schematic of the preparation of the TaON/CdS composites.

#### 2.4. General Characterization

XRD characterization was performed to determine the composition, crystal structure, and the purity of the materials using Phillips X'Pert Multipurpose X-ray Diffraction System (MPD) with Cu-K $\alpha$  radiation in the  $2\theta$  range from  $5^\circ$  to  $80^\circ$ , at a scan rate of  $5^\circ \text{ min}^{-1}$ . The morphologies of the products were recorded by SEM images (Zeiss field emission scanning electron microscope), TEM images (FEI tecnai G20 operated at an accelerated voltage of 100 kV), and high-resolution TEM (HRTEM, JEOL JEM-3010 with an accelerated voltage of 200 kV). XPS spectra were obtained via a Physical Electronics PHI 5000 Versa probe spectrometer with Al K $\alpha$  radiation (1468 eV). The as-prepared powders were dispersed in DI water by ultrasound in 1-cm quartz cells, and then placed in a UV-vis spectrophotometer to scan the UV-vis absorption spectra. The BET surface area was determined using the N<sub>2</sub> adsorption isotherms, measured by an ASAP 2020 nitrogen adsorption apparatus (Micromeritics Instruments, Norcross, USA).

#### 2.5. Photoelectrochemical Testing

The relevant photoelectrochemical analysis of this work was achieved on an electrochemical work station (CHI660E, Shanghai, China) by using a three-electrode system. In this system, the Ag/AgCl electrode was selected as the reference electrode and Pt-wire electrode was used as the counter electrode. The working electrode was fabricated by painting the suspension (4 mg of photocatalysts dispersed in 1 mL of ethanol and 10  $\mu\text{L}$  of Nafion solution) onto the FTO glass with a fixed area of  $2 \text{ cm} \times 2 \text{ cm}$ . Electrochemical impedance spectroscopies (EIS) were carried out in 0.5 M Na<sub>2</sub>SO<sub>4</sub> solution, with a frequency range of 0.01– $10^5$  Hz. The transient photocurrent measurements (*i*-T curves) were accomplished in time-dependent light–darkness cycles at a bias potential of 0.3 V. The Mott–Schottky curve (MS) was measured at a frequency of 500, 800 and 1000 Hz using this three-electrode system.

#### 2.6. Photocatalytic Hydrogen Production

The photocatalytic H<sub>2</sub> evolution performances of the prepared photocatalysts were evaluated by a commercial test system (LabSolar 6A systems, Perfect Light, Beijing, China) connected to gas chromatography (Tianmei, GC7900), equipped with a TCD detector and 5 Å molecular sieve column, as shown in Figure S1. A vacuum was required for the test system and Ar was used as the carrier gas. For photocatalysis, 10 mg of the prepared TaON/CdS composites were dispersed in the 90-mL solution, containing 10 mL lactic acid (as a sacrificial agent) aqueous solution with 2 wt% Pt cocatalyst. After stirring, the solution was then transferred into an externally illuminated photocatalytic reactor with a 300 W Xe lamp (PLS-SXE300, Perfect Light, Beijing, China) as a light source. The lamp with a cut-off filter ( $\lambda > 420 \text{ nm}$ ) was placed 7 cm above the reactor. The temperature of the reactor was kept at  $5^\circ \text{C}$  using the recycled cooling water. The generated H<sub>2</sub> was sent for gas chromatography every 0.5 h for qualitative and quantitative analysis. The apparent quantum yield value (AQY) of the catalyst for H<sub>2</sub> evolution was measured by various

single bandpass filters ( $420 \pm 5$ ,  $475 \pm 5$ ,  $550 \pm 5$ , and  $650 \pm 5$  nm). In addition the AQY values were calculated by the following equation [29]:

$$\begin{aligned} \text{quantum yield} &= \frac{\text{number of reacted electrons}}{\text{number of incident photons}} \times 100\% \\ &= \frac{2 \times \text{number of evolved H molecules}}{\text{number of incident photons}} \times 100\% \\ &= \frac{2 \times N_{H_2}}{N_i} \times 100\% \\ &= \frac{2 \times N_{H_2}}{\frac{I \times A \times t \times \lambda}{h \times c}} \times 100\% \end{aligned} \quad (1)$$

where  $N_{H_2}$  refers to the amount of hydrogen produced;  $I$  refers to the illumination intensity ( $I = 6.16$  mW/cm<sup>2</sup>;  $A$  is the illumination area ( $A = 16$  cm<sup>2</sup>);  $t$  is the irradiation time, ( $t = 3600$  s);  $\lambda$  represents the optical wavelength ( $\lambda = 420$  nm);  $h$  is Planck's constant ( $h = 6.62 \times 10^{-34}$  J·s);  $c$  is the speed of light ( $c = 3 \times 10^8$  m/s).

### 3. Results and Discussion

#### 3.1. Catalyst Characterization

The crystal structures of the pristine TaON particles, CdS nanoparticles, and the composites (TC2, TC4 and TC6) were characterized by XRD, as shown in Figure 1. The pattern at the bottom of the figure was indexed to the monoclinic phase TaON (PDF#01-070-1193), while the red pattern was assigned to the hexagonal phase CdS (PDF#01-080-0006). The sharp peaks indicate that the pristine CdS and TaON particles were well crystallized. In the patterns of the composites, the majority of the diffraction peaks were indexed to the CdS particles, suggesting that CdS was the dominant material in the composites. The TaON peaks exhibited much lower intensities than that of CdS, indicating the low content of TaON. No impurity peak was found in the composites, indicating that the hydrothermal process did not change the phase of TaON and CdS.

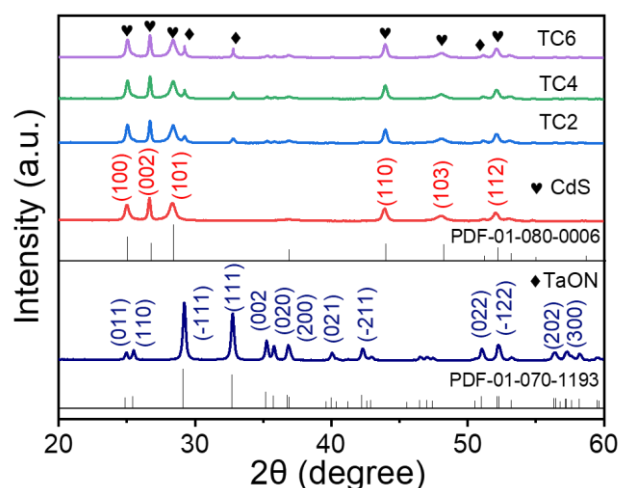
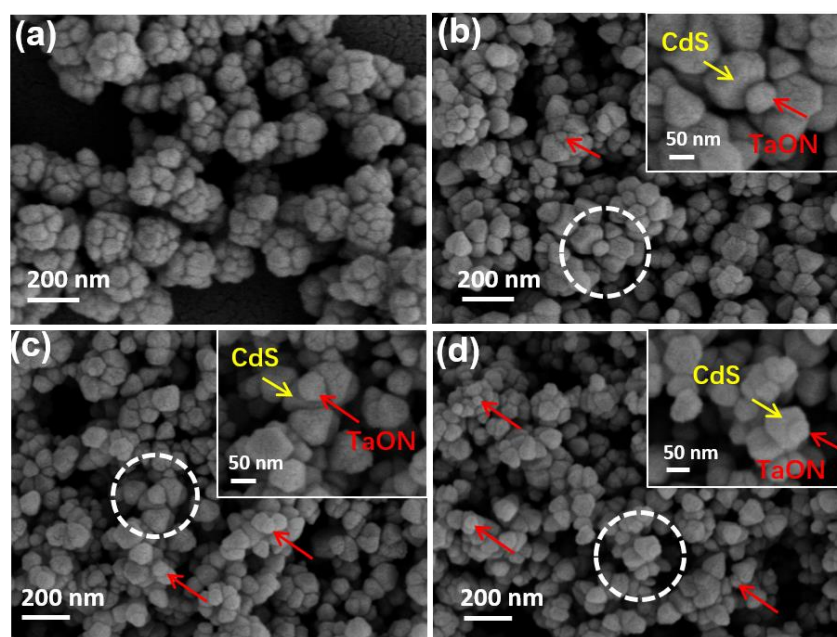


Figure 1. The XRD patterns of CdS, TaON, TC2, TC4 and TC6 samples.

The morphology of the as-prepared samples was investigated by SEM and TEM. As shown in Figure 2a, the pristine CdS microparticles with a diameter of ~200 nm were aggregated by CdS hexagonal nanoparticles (~100 nm). The pristine TaON showed a smaller sphere-like structure with a diameter of 50–70 nm, as shown in Figure S2. Figure 2b–d present the SEM images of TC2–6. To clearly distinguish the TaON and CdS particles, an inset of the enlarged area (white circle) is provided in each SEM of the samples. In these insets, the TaON and CdS particles are marked by arrows based on their shapes and sizes. As the amount of TaON increased, the aggregated CdS microspheres were decomposed into individual CdS nanoparticles, and more TaON particles were attached to the surface of CdS particles.



**Figure 2.** SEM image of (a) the CdS nanoparticles; (b) the TC2, (c) TC4 and (d) TC6 composites. The insets in (b–d) are the zoomed-in SEM images in the white circles.

Figure 3a shows the TEM image of the pristine CdS nanoparticles. Discrete particles with hexagonal and irregular shapes ( $\sim 100$  nm) were observed. The irregular CdS nanoparticles with edges were probably generated from the hexagonal particles by Ostwald ripening in the hydrothermal process. The prepared TaON showed a near spherical shape with a relatively smooth surface (Figure 3b). The selected area electron diffraction (SAED) patterns of the pristine CdS and TaON are displayed in the insets of Figure 3a,b, respectively. The well-aligned diffraction spots of (100), (110) and (010) planes were observed in the SAED of CdS, revealing that the CdS was a single-crystal hexagonal structure. The diffraction dots of the pristine TaON were indexed to the (110) and (100) planes. The extra electron diffraction spots were caused by the neighboring particles. Figure 3c displays the TEM image of the TC4 composites, suggesting that the TaON particles were attached to the CdS particles. An HRTEM image was taken at the interface between TaON and CdS in the TC4 composites, as presented in Figure 3d. The intimate contact between the two materials was observed, indicating that the heterojunction was formed. The lattice spacings of 0.28 nm and 0.36 nm were indexed to the (011) plane of TaON and the (111) plane of CdS. Figure 4 shows the elemental mapping of the contact area of TaON and CdS in the TC4 composites to characterize the element distribution of the five elements (Cd, S, Ta, O and N). The STEM image of the contact area is shown in Figure 4a. Figure 4b–f exhibit the individual element distribution of Cd, S, Ta, O and N, proving that the TaON nanospheres were decorated on the surface of the CdS nanoparticles.

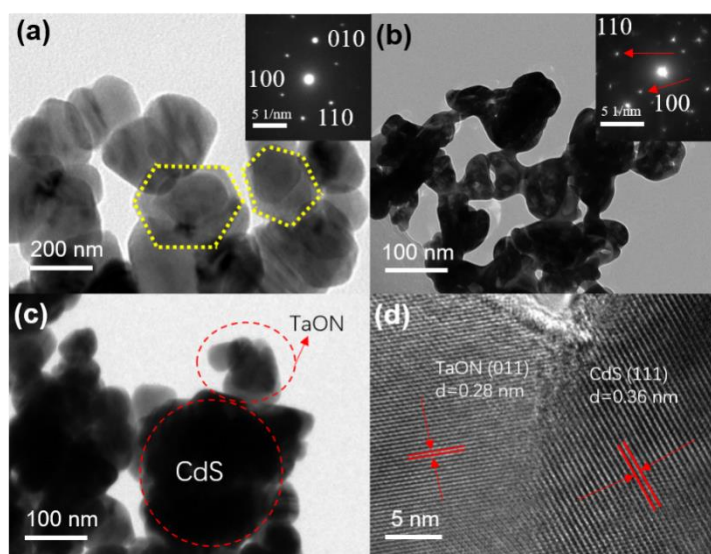


**Figure 3.** (a) TEM images of the pristine CdS nanoparticles (the yellow circles indicate the hexagonal particles of CdS), (b) the TaON particles (the corresponding SEADs are shown in the inset), and (c) the TC4 composites; (d) HRTEM image of the interface of CdS and TaON in the TC4 composite.

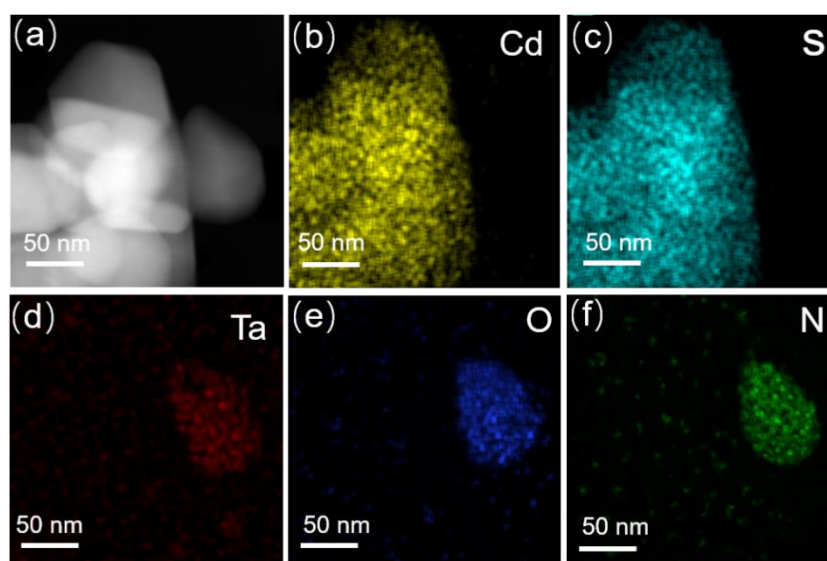


**Figure 4.** (a) STEM image of the TC4 nanocomposites and the corresponding EDS mapping of (b) Cd, (c) S, (d) Ta, (e) O, (f) N.

The XPS was performed to study the chemical composition and surface electron state of the elements in the pristine materials and the TC4 nanocomposites, as shown in Figure 5. Figure 5a displays the XPS surveys of the pristine CdS and TC4 composites. Only Cd, S, O and C elements were observed in the spectrum of the pristine CdS, where the C1s peak located at 284.6 eV was indexed to the reference C for calibration. In the survey of the TC4 composites, the peaks included the elements of Ta, O, N, Cd, and S. Figure 5b depicts the high-resolution spectra of Cd 3d in the pristine CdS and TC4. The Cd 3d<sub>5/2</sub> and Cd 3d<sub>3/2</sub> in the Cd 3d spectrum were located at 404.6 eV and 411.4 eV, suggesting the existence of Cd<sup>2+</sup>. In the spectrum of the composites, the two peaks shifted 0.1 eV towards low energy. Only one fitted peak in the spectra reveals that no other valency of Cd existed. The high-resolution spectra of S in the pristine CdS and the TC4 composites are shown in Figure 5c. Two peaks were fitted in the spectra, corresponding to the S 2P<sub>3/2</sub> and S 2P<sub>1/2</sub>. A 0.2-eV shift to low energy was observed in these peaks. The Ta spectra

are presented in Figure 5d, in which the pristine TaON was added for comparison. The Ta 4f<sub>7/2</sub> and Ta 4f<sub>5/2</sub> peaks in the TC4 composites were found at 24.9 eV and 26.8 eV, and the binding energy was 0.1 eV lower than that of pristine TaON. The O1s peaks in the two materials showed similar asymmetric peaks. The main peak at ~529.8 eV was indexed to the lattice oxygen in the TaON crystal structure, while the other one located at 531.5 eV can be attributed to the O vacancy. A similar scenario occurred in N spectra. The single peak located at 395.9 eV belonged to the N 1s peak (Figure 5f). A binding energy shift to low energy after modification happened in the XPS spectra of these elements, indicating the interfacial electron transfer from CdS to TaON [30]. This phenomenon also proved that the heterojunctions between the two materials formed, implying the enhanced photocatalytic performance of the prepared composites.

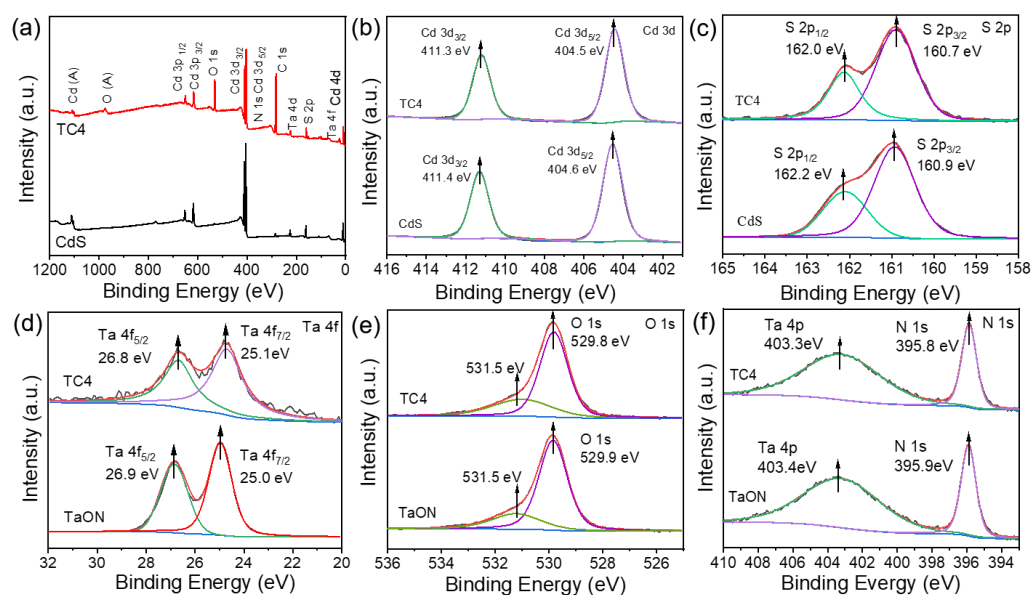


**Figure 5.** XPS spectra of CdS, TaON and TC4 samples: (a) survey, (b) Cd 3d, (c) S 2p, (d) Ta 4f, (e) O 1s, (f) N 1s.

UV–vis optical spectroscopy was used to investigate the light-harvesting abilities of the prepared samples. Figure 6a shows the UV–vis absorption spectra of the pristine TaON, CdS and various composites (TC2, 4, and 6). The absorption band edges of the pristine TaON and CdS were located at about 450 nm and 500 nm, respectively. Compared with the pristine samples, the composites exhibited a wider and stronger absorption peak. The red-shifts of the absorption peaks of the CdS/TaON composites indicate the better utilization of solar light when forming heterojunctions. Furthermore, the intensities in the visible light range also increased for the composites. This also confirms that the light adsorption of the composites in the visible range increased. The highest absorption intensity from 550–800 nm was observed in TC4 but decreased in TC6. This is probably due to the shielding effect induced by excessive TaON, which hampered the light absorption of CdS [31,32]. To characterize the bandgaps of the TaON and CdS, Tauc plots of the two pristine materials were drawn based on the UV–vis adsorption spectra, as shown in Figure 6b. The Tauc plots, used to calculate the bandgaps of the samples based on the UV–vis adsorption spectra, were quantitatively acquired from the following equation [33]:

$$(\alpha h\nu)^2 = A (h\nu - E_g) \quad (2)$$

where  $\alpha$ ,  $h$ ,  $\nu$ ,  $E_g$  and  $A$  are the absorption coefficient, Planck constant, light frequency, bandgap and constant, respectively. The bandgaps of the pristine CdS nanoparticles and TaON particles were calculated to be 2.64 eV and 2.38 eV, respectively, in good agreement with the literature [34,35].

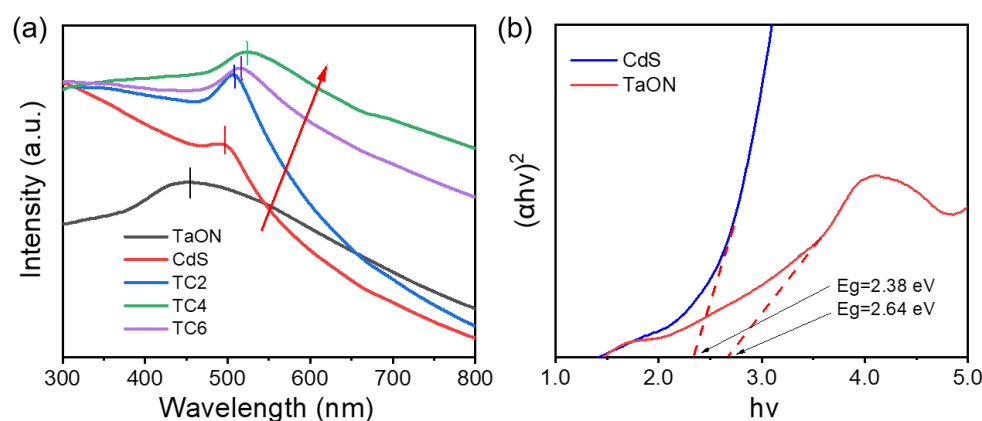


**Figure 6.** (a) UV-vis absorption spectra of TaON, CdS, TC2, TC4 and TC6 samples; (b) Tauc plots of the pristine TaON and CdS samples.

### 3.2. Photocatalytic Performance Tests

To verify the influence of the catalyst dose of the photocatalysts on photocatalytic hydrogen performance, the experiments with the different initial concentrations of the TaON/CdS nanocomposites were firstly carried out under visible light irradiation. As shown in Figure S3, the highest hydrogen production performance ( $19.18 \text{ mmol g}^{-1} \text{ h}^{-1}$ ) was found at the catalyst concentration of  $0.1 \text{ g L}^{-1}$ . Therefore, we selected  $0.1 \text{ g L}^{-1}$  of catalysts to evaluate the photocatalytic performance in this study. Photocatalytic hydrogen production over the pristine CdS and TaON/CdS nanocomposites was evaluated under visible light irradiation. Figure 7a shows the photocatalytic  $\text{H}_2$  evolution rates of the as-prepared photocatalysts. The composites exhibited higher  $\text{H}_2$  evolution rates than the pristine CdS nanoparticles. The highest hydrogen production rate ( $19.29 \text{ mmol g}^{-1} \text{ h}^{-1}$ ) was found in TC4 composites, which was 2.13 times higher than that of the unmodified CdS nanoparticles ( $9.03 \text{ mmol g}^{-1} \text{ h}^{-1}$ ). The corresponding time-dependent  $\text{H}_2$  evolution rates of the as-prepared photocatalysts are shown in Figure 7b. The produced  $\text{H}_2$  evolution amounts of the pristine CdS particles and the composites steadily increased with time, while the pristine TaON showed little photocatalytic activity under visible light irradiation. When the TaON nanospheres were loaded with the CdS nanoparticles, a heterojunction was established, accelerating the separation and charge transfer of the generated electron-hole pairs. The cycle stability tests of the pristine CdS and the TC4 composites were also evaluated, as depicted in Figure 7c. The result of the 4-cycle test demonstrates that the composites exhibited much better catalytic stability. The poor stability of the pristine CdS may be caused by the photo-corrosion that originates from the reduction of surface sulfur ions. The formation of the heterojunction led to the transfer of the photo-generated electrons to TaON, which enables them to suppress the photo-corrosion. The SEM and XRD of TC4 (Figure S6) after the cycle stability test indicate that the morphology and crystal structure of TC4 changed only slightly. Figure 7d shows the apparent quantum yield (AQY) of the TC4 sample under various single wavelength irradiations and the corresponding UV-vis absorption spectrum was provided for comparison. The AQY has been calculated to be 18.23% at 420 nm, 22.13% at 470 nm, 3.25% at 550 nm and 0.42% at 650 nm, respectively. The photocatalytic  $\text{H}_2$  performances of some reported CdS-based photocatalysts with different co-catalysts are summarized in Table 1. It can be concluded that the TaON/CdS composites prepared in this work exhibit better photocatalytic  $\text{H}_2$  evolution rates and AQY values.

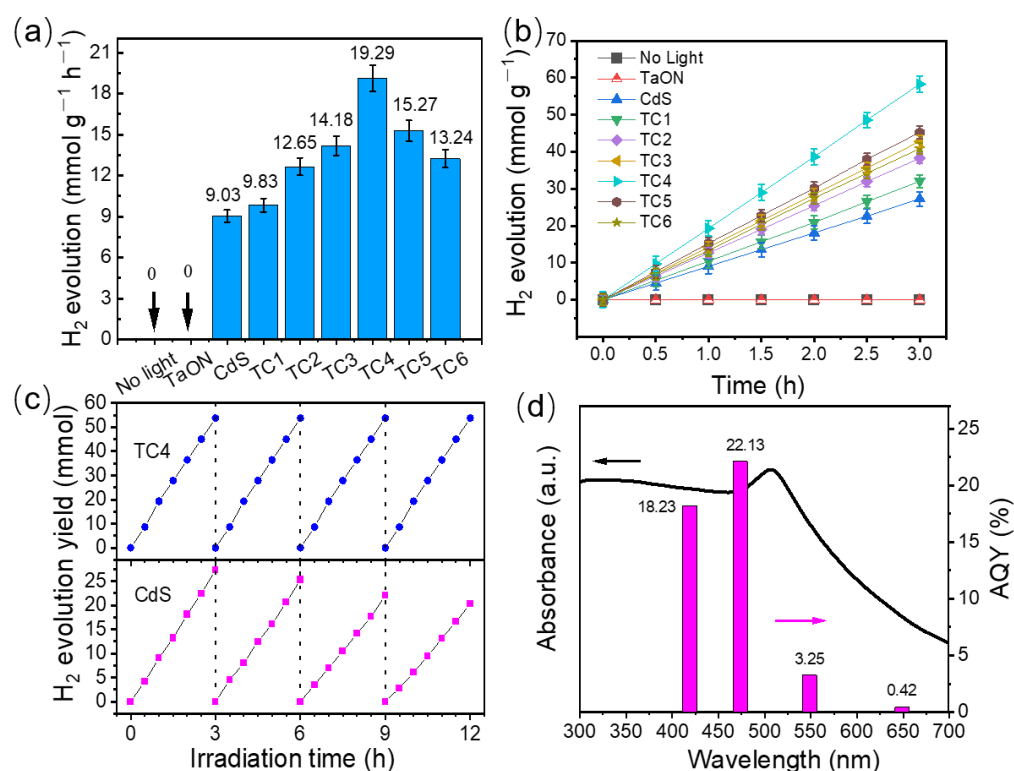


**Figure 7.** (a,b) The photocatalytic activities of pristine CdS and TC1-TC6 samples. (c) Recycle runs of H<sub>2</sub> evolution of pristine CdS and TC4 composites. (d) AQY versus UV-vis adsorption spectrum of TC4 composites.

**Table 1.** The photocatalytic HER performances of various CdS-based catalysts.

Photocatalysts	Light Source	Sacrificial Reagent	Activity (mmol g <sup>-1</sup> h <sup>-1</sup> )	AQY (420 nm)	References
TaON /CdS hybrids	$\lambda > 420$ nm	10% lactic acid	19.29	18.23%	This work
MoS <sub>2</sub> /CdS nanocrystals	$\lambda > 420$ nm	10% TEOA	1.15	0.66%	[36]
C-doped CdS nanoparticles @Graphene	AM 1.5G	0.125 M Na <sub>2</sub> S 0.15 M Na <sub>2</sub> SO <sub>3</sub>	3.12	11.7%	[37]
CdS nanorods /ZnS nanosheets	$\lambda > 420$ nm	0.025 M NaH <sub>2</sub> PO <sub>2</sub>	9.44	/	[38]
CuO /CdS nanorods	$\lambda > 420$ nm	8% lactic acid	3.317	6.3%	[39]
NiS /CdS nanorods	$\lambda > 420$ nm	0.35 M Na <sub>2</sub> S 0.25 M Na <sub>2</sub> SO <sub>3</sub>	1.131	6.1%	[40]
mesoporous SiO <sub>2</sub> /SiO <sub>2</sub> -derived	$\lambda > 420$ nm	10% TEOA	0.607	/	[41]
g-C <sub>3</sub> N <sub>4</sub> @CdS	$\lambda > 420$ nm	10% TEOA	2.73	/	[42]

### 3.3. Photocatalytic Mechanism Analysis

To deeply understand the underlying reasons for the enhanced photocatalytic performances of the as-prepared catalysts, several electrochemical measurements were conducted. Figure S4 shows the transient photocurrent of TaON, CdS, and a series of the composites with the light on/off period under visible light irradiation. The photocurrent density of the pristine TaON was quite low, which may be the reason for the negligible HER performance of TaON. The CdS particles also exhibited a low response but better than that of TaON.

The photocurrent intensities of the composites were much higher than that of the pristine CdS, indicating that the decoration of TaON induces extra photogenerated charges. The TC4 nanocomposites showed the highest photocurrent density, implying more photoelectrons were generated to participate in the hydrogen evolution reaction. Electrochemical impedance spectroscopy (EIS) was used to further evaluate the charge transfer ability and separation efficiency of the as-prepared photocatalyst. In the EIS Nyquist plots (Figure 8a), the pristine TaON and CdS particles showed larger arc diameters, indicating higher charge transfer resistance. The smallest arc diameter was found at the TC4 sample, suggesting the best charge transfer ability among the samples. To quantitatively compare the charge transfer properties, an equivalent circuit was used to fit the EIS plots (the inset in Figure 8a).  $R_{ct}$  represents the charge transfer resistance between the electrodes and solution;  $R_s$  is the solution resistance and CPE corresponds to the double layer capacitor for the constant phase element. Table 2 lists the fitting results of  $R_s$ ,  $R_{ct}$  and CPE of the pristine TaON and CdS, and TC2-6 samples. The TC4 sample exhibited similar  $R_s$  and CPE but the smallest  $R_{ct}$  ( $1.71 \times 10^5 \Omega$ ), implying that the TC4 may possess higher photocatalytic HER performance.

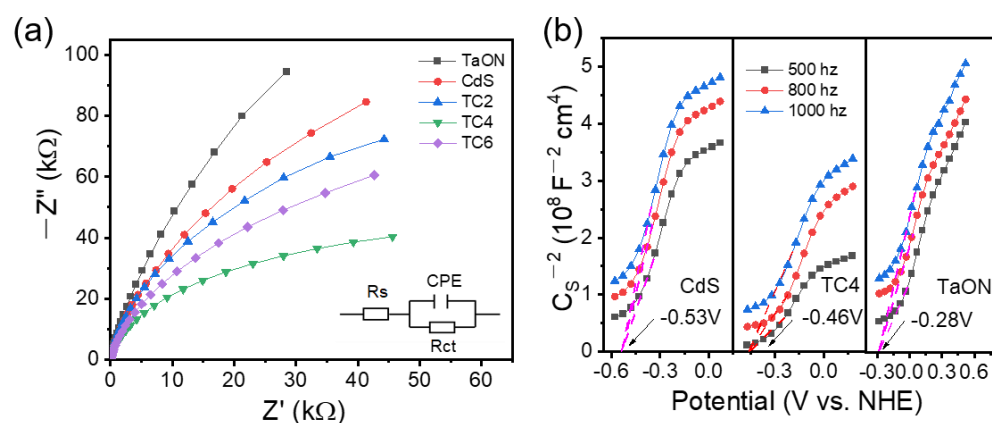


**Figure 8.** (a) Electrochemical impedance spectra (EIS) of pristine TaON, CdS, and the composite samples; (b) Mott–Schottky plots of the samples.

**Table 2.** The fitted resistances of the prepared samples based on the equivalent circuits.

Samples	$R_{ct}$ ( $\Omega$ )	$R_s$ ( $\Omega$ )	CPE ( $\mu\text{F}$ )
CdS	$6.02 \times 10^5$	6.65	121.4
TaON	$8.63 \times 10^5$	8.52	211.3
TC2	$4.28 \times 10^5$	7.59	124.2
TC4	$1.71 \times 10^5$	6.06	122.3
TC6	$3.35 \times 10^5$	7.62	125.7

The Mott–Schottky curves were measured to verify the flat-band potential and compare the concentrations of charge carriers of the pristine CdS, TaON particles, and the TC4 composites. As shown in Figure 8b, the slopes of the Mott–Schottky diagram of the samples were positive, indicating that the three samples were typical *n*-type semiconductors. The flat band potentials of the pristine CdS nanoparticles, TaON particles and the TC4 nanocomposites were estimated to be  $-0.53$  V,  $-0.28$  V and  $-0.46$  V (vs. NHE). In addition, it is well accepted that the conduction band potential is negative  $\sim 0.1$  eV compared to the flat band potential for *n*-type semiconductors. Therefore, the conduction band ( $E_{CB}$ ) potentials ( $E_{CB}$ ) of the pristine CdS nanoparticles, TaON particles and TC4 nanocomposites were calculated to be  $-0.63$  V,  $-0.38$  V and  $-0.56$  V (vs. NHE). In addition, the valence band potential ( $E_{VB}$ ) could be calculated by the following formula [43]:  $E_{VB} = E_{CB} + E_g$ . Combined with the results of the Tauc plots, the valence bands of the pristine CdS and TaON particles were 1.75 V and 2.26 V. Based on the calculation, the band structures of CdS and TaON

can be drawn, as shown in Figure 9. Moreover, the donor densities of the three samples can be qualitatively estimated by the slopes of the Mott–Schottky plots. The smaller slope represents the larger donor density. The slopes of the tangent lines in the Mott–Schottky plots (Figure 8b, 800 Hz) were calculated as  $5.67 \times 10^8$ ,  $4.76 \times 10^8$ ,  $2.03 \times 10^8$  for the pristine CdS nanoparticles, the TaON particles, and the TC4 nanocomposites, respectively. The donor density of the composites was higher than those of the pristine CdS and TaON, indicating that the composites possessed the enhanced photocatalytic properties. Furthermore, nitrogen adsorption isotherms were used to investigate the specific surface areas and pore structures of the samples. As shown in Figure S5, the adsorption–desorption isotherms of the samples were typical type IV isotherms. The BET surface areas of TaON, CdS, and TC4 were calculated to be 5.22, 10.26 and 26.82  $\text{m}^2 \text{g}^{-1}$ . In comparison to the pristine CdS, the specific surface area of TC4 composites slightly increased, suggesting that the specific surface area may be a factor for enhancing the photocatalytic activity.

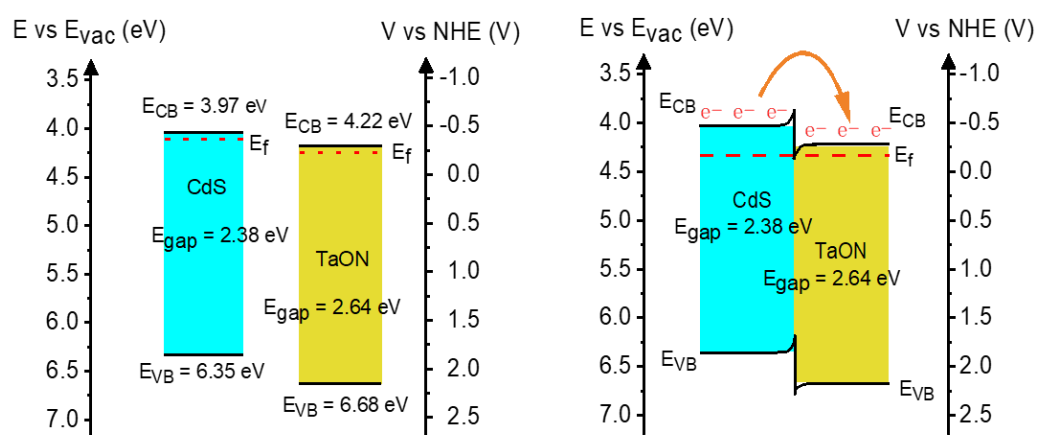


**Figure 9.** Schematic illustration of photocatalytic mechanism of TaON/CdS nanocomposites under visible light irradiation.

The band structures of the pristine TaON and CdS nanoparticles and the possible transfer mechanism of charge carriers between the heterojunction of the TaON/CdS system are illustrated in Figure 9. Under visible light irradiation, the photogenerated electrons were excited from the VB to the conduction band of CdS and led to the generation of a photocurrent, which was proved by the photocurrent transient response (Figure S4). The holes remained at the VB of CdS. The pristine CdS exhibited low photocatalytic activities, probably due to the fast recombination of the photo-excited charge carriers that arose from the inherent defects of the CdS photocatalysts. Benefitting from the fabrication of the TaON/CdS heterojunction, the photogenerated electrons produced from CdS transferred to TaON due to the band bending of the heterostructures, and then combined with the absorbed  $\text{H}^+$  to generate  $\text{H}_2$ . The positive holes created in the VB of CdS were trapped by the sacrificial agent (lactic acid). This process reduces the recombination rate and leads to more electrons combining with  $\text{H}^+$  to produce  $\text{H}_2$ , which is confirmed by the photo-response current (Figure S3). Furthermore, the presence of the cocatalyst TaON enhances the transfer of charge carriers (Figure 8a), and increases the electron density (Figure 8b). In addition, the decoration of TaON enhances the adsorption of visible light (Figure 6a). In summary, establishing heterojunctions between CdS and TaON is critical for the enhancement of catalytic activity, attributed to the following three reasons: (1) inhibiting the recombination of photogenerated electron–hole pairs, (2) increasing the absorption of light, and (3) generating more photogenerated electrons combined with  $\text{H}^+$  to produce  $\text{H}_2$ .

In addition, we think that the highest photocatalytic performance of TC4 is strongly related to the suitable decoration amount of TaON. As shown in Figure 2b–d, the CdS microspheres (see Figure 2a) gradually decomposed into CdS nanoparticles. This process increased the active surface of CdS and the surface where a heterojunction can form

with TaON. Less decorated TaON particles cannot provide sufficient heterojunctions (TC2, Figure 2b). Excessive TaON particles on the CdS surface (TC6, Figure 2d) may block the light absorption of CdS and decrease the activity [31]. Only a suitable amount and distribution of TaON on CdS provide optimized photocatalytic activity.

#### 4. Conclusions

In this study, high-performance and stable TaON/CdS nanocomposites were successfully fabricated by a one-step hydrothermal method with the existence of TaON particles. Various mass ratios of CdS to TaON (TC-2, 10 wt%; TC-4, 20 wt%, and TC-6, 30 wt%) were optimized, according to the performance of photocatalytic hydrogen production. Among the composites, TC4 exhibited the highest photocatalytic hydrogen evolution rate ( $19.29 \text{ mmol g}^{-1} \text{ h}^{-1}$ ) among these samples, which was 2.13 times higher than that of the pristine CdS ( $9.03 \text{ mmol g}^{-1} \text{ h}^{-1}$ ). Moreover, the apparent quantum yield (AQY) of photocatalytic  $\text{H}_2$  evolution reached 18.23% at 420 nm. The enhanced photocatalytic hydrogen efficiency was ascribed to the construction of the TaON/CdS heterojunction, leading to increased active sites, the effective separation and low recombination rate of photogenerated charges, the small transfer resistance of photoelectrons, and enhanced stability. This work provides new insights into designing the construction of CdS-based photocatalysts in realizing highly efficient photocatalytic hydrogen evolution.

**Supplementary Materials:** The following supporting information can be downloaded at: <https://www.mdpi.com/article/10.3390/catal12101110/s1>, Figure S1: Commercial photocatalytic water splitting system; Figure S2: SEM image of the TaON nanoparticles; Figure S3: Photocatalytic  $\text{H}_2$  evolution rate of the different initial concentrations of the TC4 composites; Figure S4: Transient photocurrent responses of pristine TaON, CdS, and the composites samples; Figure S5: the  $\text{N}_2$  sorption isotherm of the TaON nanospheres, the CdS nanoparticles and the TC4 composites; Figure S6: (a) SEM image of the TC4 nanocomposites after the cycle stability test; (b) XRD images of the TC4 nanocomposites before and after the cycle stability test. Table S1: The elemental composition of Ta and Cd measured by ICP-AES; Table S2: The surface areas and pore sizes of the CdS nanoparticles, the TaON nanospheres and the TC4 composites.

**Author Contributions:** Writing original draft and methodology, F.C.; Conceptualization and formal analysis, H.F.; writing review and editing, X.Y.; and resources S.X. and X.A. All authors have read and agreed to the published version of the manuscript.

**Funding:** This research was funded by the National Nature Science Foundation of China grant number [No. 51974086] and the Fundamental Research Funds for the Central Universities grant number [N2125027, N2225028 and N2124007-1].

**Data Availability Statement:** The data presented in this study are available upon request from the corresponding author.

**Acknowledgments:** We acknowledge the financial support from the National Nature Science Foundation of China (No. 51974086) and the Fundamental Research Funds for the Central Universities (N2125027, N2225028 and N2124007-1). Special thanks are given to the instrumental and data analysis by the Analytical and Testing Center, Northeastern University. The authors also thank Shiyanjia Lab ([www.shiyanjia.com](http://www.shiyanjia.com)) (accessed on 15 September 2022) for the XPS measurements.

**Conflicts of Interest:** The authors declare no conflict of interest.

#### References

1. Hou, J.G.; Wang, Z.; Kan, W.B.; Jiao, S.Q.; Zhu, H.M.; Kumar, R.V. Efficient visible-light-driven photocatalytic hydrogen production using CdS@TaON core-shell composites coupled with graphene oxide nanosheets. *J. Mater. Chem.* **2012**, *22*, 7291–7299. [[CrossRef](#)]
2. Zou, Y.Y.; Guo, C.Y.; Cao, X.L.; Zhang, L.G.; Chen, T.X.; Guo, C.; Wang, J.D. Synthesis of CdS/CoP hollow nanocages with improved photocatalytic water splitting performance for hydrogen evolution. *J. Environ. Chem. Eng.* **2021**, *9*, 106270. [[CrossRef](#)]
3. Lei, Y.; Wu, X.; Li, S.; Huang, J.; Ng, K.H.; Lai, Y. Noble-metal-free metallic MoC combined with CdS for enhanced visible-light-driven photocatalytic hydrogen evolution. *J. Clean. Prod.* **2021**, *322*, 129018. [[CrossRef](#)]

4. Sun, G.; Xiao, B.; Shi, J.-W.; Mao, S.; He, C.; Ma, D.; Cheng, Y. Hydrogen spillover effect induced by ascorbic acid in CdS/NiO core-shell p-n heterojunction for significantly enhanced photocatalytic H<sub>2</sub> evolution. *J. Colloid Interface Sci.* **2021**, *596*, 215–224. [[CrossRef](#)]
5. El-Hakam, S.A.; Alshorifi, F.T.; Salama, R.S.; Gamal, S.; El-Yazeed, W.S.A.; Ibrahim, A.A.; Ahmed, A.I. Application of nanostructured mesoporous silica/ bismuth vanadate composite catalysts for the degradation of methylene blue and brilliant green. *J. Mater. Res. Technol.* **2022**, *18*, 1963–1976. [[CrossRef](#)]
6. Alshorifi, F.T.; Alswat, A.A.; Mannaa, M.A.; Alotaibi, M.T.; El-Bahy, S.M.; Salama, R.S. Facile and Green Synthesis of Silver Quantum Dots Immobilized onto a Polymeric CTS-PEO Blend for the Photocatalytic Degradation of p-Nitrophenol. *ACS Omega* **2021**, *6*, 30432–30441. [[CrossRef](#)]
7. Alshorifi, F.T.; Ali, S.L.; Salama, R.S. Promotional Synergistic Effect of Cs-Au NPs on the Performance of Cs-Au/MgFe<sub>2</sub>O<sub>4</sub> Catalysts in Catalysis 3,4-Dihydropyrimidin-2(1H)-Ones and Degradation of RhB Dye. *J. Inorg. Organomet. Polym. Mater.* **2022**, *32*, 1–12. [[CrossRef](#)]
8. Gai, Q.; Zheng, X.; Liu, W.; Dong, Q.; Wang, Y.; Gao, R.; Ren, S. 2D-2D heterostructured CdS-CoP photocatalysts for efficient H<sub>2</sub> evolution under visible light irradiation. *Int. J. Hydrog. Energy* **2019**, *44*, 27412–27420. [[CrossRef](#)]
9. Zhong, W.W.; Tu, W.G.; Feng, S.S.; Xu, A.J. Photocatalytic H<sub>2</sub> evolution on CdS nanoparticles by loading FeSe nanorods as co-catalyst under visible light irradiation. *J. Alloy. Compd.* **2019**, *772*, 669–674. [[CrossRef](#)]
10. Wu, T.F.; Huang, J.F.; Cheng, G.; Pang, Y.W. Enhanced photocatalytic hydrogen evolution based on ternary noble-metal-free Co<sub>3</sub>O<sub>4</sub>/CdS/g-C<sub>3</sub>N<sub>4</sub> composite. *Mater. Lett.* **2021**, *292*, 129274. [[CrossRef](#)]
11. An, L.; Han, X.; Li, Y.G.; Hou, C.Y.; Wang, H.Z.; Zhang, Q.H. ZnS-CdS-TaON nanocomposites with enhanced stability and photocatalytic hydrogen evolution activity. *J. Sol-Gel Sci. Technol.* **2019**, *91*, 82–91. [[CrossRef](#)]
12. Zhu, R.S.; Yang, R.J.; Hu, L.J.; Chen, B.Y. Preparation of Z-Scheme system of CdS-RGO-BiVO<sub>4</sub> and its activity for hydrogen production. *Int. J. Hydrog. Energy* **2019**, *44*, 25119–25128. [[CrossRef](#)]
13. Yuan, M.; Zhou, W.H.; Kou, D.X.; Zhou, Z.J.; Meng, Y.N.; Wu, S.X. Cu<sub>2</sub>ZnSnS<sub>4</sub> decorated CdS nanorods for enhanced visible-light-driven photocatalytic hydrogen production. *Int. J. Hydrog. Energy* **2018**, *43*, 20408–20416. [[CrossRef](#)]
14. Xu, Y.; Yan, A.; Jiang, L.; Huang, F.; Hu, D.; Duan, G.; Zheng, F. MoS<sub>2</sub>/HCSs/ZnIn<sub>2</sub>S<sub>4</sub> nanocomposites with enhanced charge transport and photocatalytic hydrogen evolution performance. *J. Alloy. Compd.* **2022**, *895*, 162504. [[CrossRef](#)]
15. Kumar, D.P.; Seo, S.; Rangappa, A.P.; Kim, S.; Joshi Reddy, K.A.; Gopannagari, M.; Bhavani, P.; Reddy, D.A.; Kim, T.K. Ultrathin layered Zn-doped MoS<sub>2</sub> nanosheets deposited onto CdS nanorods for spectacular photocatalytic hydrogen evolution. *J. Alloy. Compd.* **2022**, *905*, 164193. [[CrossRef](#)]
16. Wei, T.T.; Jin, Z.B.; Li, F.Y.; Yan, D.D.; Xu, L. Efficient visible-light-driven photocatalytic hydrogen production over a direct Z-scheme system of TaON/Cd<sub>0.5</sub>Zn<sub>0.5</sub>S with a NiS cocatalyst. *Photochem. Photobiol. Sci.* **2020**, *19*, 80–87. [[CrossRef](#)]
17. Zhu, Y.; Liu, Y.; Ai, Q.; Gao, G.; Yuan, L.; Fang, Q.; Tian, X.; Zhang, X.; Egap, E.; Ajayan, P.M. In Situ Synthesis of Lead-Free Halide Perovskite-COF Nanocomposites as Photocatalysts for Photoinduced Polymerization in Both Organic and Aqueous Phases. *ACS Mater. Lett.* **2022**, *4*, 464–471. [[CrossRef](#)]
18. Yin, X.-L.; Liu, J.; Jiang, W.-J.; Zhang, X.; Hu, J.-S.; Wan, L.-J. Urchin-like Au@CdS/WO<sub>3</sub> micro/nano heterostructure as a visible-light driven photocatalyst for efficient hydrogen generation. *Chem. Commun.* **2015**, *51*, 13842–13845. [[CrossRef](#)] [[PubMed](#)]
19. Hao, X.; Hu, Z.; Xiang, D.; Jin, Z. Construction of CdS@Cu<sub>2</sub>-xS core-shell p-n heterojunction with enhanced charge separation for wide spectrum photocatalytic H<sub>2</sub> evolution. *Mol. Catal.* **2022**, *528*, 112417. [[CrossRef](#)]
20. Liu, S.; Xiao, W.; Jin, C.; Xia, S.; Wang, W.; Jiang, X.; Li, L.; Wang, S.; Chen, C. MOFs derived CdS/CdO heterojunction photoanode for high-efficient water splitting. *Appl. Surf. Sci.* **2022**, *605*, 154697. [[CrossRef](#)]
21. Liu, C.; Ma, J.; Zhang, F.-J.; Wang, Y.-R.; Kong, C. Facile formation of Mo-vacancy defective MoS<sub>2</sub>/CdS nanoparticles enhanced efficient hydrogen production. *Colloids Surf. A: Physicochem. Eng. Asp.* **2022**, *643*, 128743. [[CrossRef](#)]
22. Han, B.; Liu, S.Q.; Zhang, N.; Xu, Y.J.; Tang, Z.R. One-dimensional CdS@MoS<sub>2</sub> core-shell nanowires for boosted photocatalytic hydrogen evolution under visible light. *Appl. Catal. B Environ.* **2017**, *202*, 298–304. [[CrossRef](#)]
23. Liu, Y.; Zhou, Y.; Chen, G.; Guo, T.; Wang, L.; Huang, X.; Zeng, W. Loading cobalt phosphate on TaON surface as efficient noble-metal-free co-catalyst for enhanced photocatalytic water oxidation performance. *Mater. Lett.* **2015**, *148*, 155–158. [[CrossRef](#)]
24. Hou, J.G.; Cheng, H.J.; Yang, C.; Takeda, O.; Zhu, H.M. Hierarchical carbon quantum dots/hydrogenated-gamma-TaON heterojunctions for broad spectrum photocatalytic performance. *Nano Energy* **2015**, *18*, 143–153. [[CrossRef](#)]
25. Chen, S.S.; Qi, Y.; Hisatomi, T.; Ding, Q.; Asai, T.; Li, Z.; Ma, S.S.K.; Zhang, F.X.; Domen, K.; Li, C. Efficient Visible-Light-Driven Z-Scheme Overall Water Splitting Using a MgTa<sub>2</sub>O<sub>6</sub>-xNy/TaON Heterostructure Photocatalyst for H<sub>2</sub> Evolution. *Angew. Chem. Int. Ed.* **2015**, *54*, 8498–8501. [[CrossRef](#)] [[PubMed](#)]
26. Chen, W.; Chu, M.C.; Gao, L.; Mao, L.Q.; Yuan, J.; Shangguan, W.F. Ni(OH)<sub>2</sub> loaded on TaON for enhancing photocatalytic water splitting activity under visible light irradiation. *Appl. Surf. Sci.* **2015**, *324*, 432–437. [[CrossRef](#)]
27. Yan, J.S.; Hu, L.Q.; Cui, L.K.; Shen, Q.Q.; Liu, X.G.; Jia, H.S.; Xue, J.B. Synthesis of disorder-order TaON homojunction for photocatalytic hydrogen generation under visible light. *J. Mater. Sci.* **2021**, *56*, 9791–9806. [[CrossRef](#)]
28. Hou, J.; Yang, C.; Wang, Z.; Ji, Q.; Li, Y.; Huang, G.; Jiao, S.; Zhu, H. Three-dimensional Z-scheme AgCl/Ag/gamma-TaON heterostructural hollow spheres for enhanced visible-light photocatalytic performance. *Appl. Catal. B Environ.* **2013**, *142*, 579–589. [[CrossRef](#)]

29. Hai, X.; Chang, K.; Pang, H.; Li, M.; Li, P.; Liu, H.M.; Shi, L.; Ye, J.H. Engineering the Edges of MoS<sub>2</sub> (WS<sub>2</sub>) Crystals for Direct Exfoliation into Monolayers in Polar Micromolecular Solvents. *J. Am. Chem. Soc.* **2016**, *138*, 14962–14969. [[CrossRef](#)]
30. Pei, L.; Yuan, Y.J.; Zhong, J.S.; Li, T.Z.; Yang, T.; Yan, S.C.; Ji, Z.G.; Zou, Z.G. Ta<sub>3</sub>N<sub>5</sub> nanorods encapsulated into 3D hydrangea-like MoS<sub>2</sub> for enhanced photocatalytic hydrogen evolution under visible light irradiation. *Dalton Trans.* **2019**, *48*, 13176–13183. [[CrossRef](#)]
31. Yin, X.-L.; Li, L.-L.; Jiang, W.-J.; Zhang, Y.; Zhang, X.; Wan, L.-J.; Hu, J.-S. MoS<sub>2</sub>/CdS Nanosheets-on-Nanorod Heterostructure for Highly Efficient Photocatalytic H<sub>2</sub> Generation under Visible Light Irradiation. *ACS Appl. Mater. Interfaces* **2016**, *8*, 15258–15266. [[CrossRef](#)] [[PubMed](#)]
32. Di, T.; Zhang, L.; Cheng, B.; Yu, J.; Fan, J. CdS nanosheets decorated with Ni@graphene core-shell cocatalyst for superior photocatalytic H<sub>2</sub> production. *J. Mater. Sci. Technol.* **2020**, *56*, 170–178. [[CrossRef](#)]
33. Yin, X.-L.; Li, L.-L.; Li, D.-C.; Li, Z.-J.; Wang, Y.-X.; Kong, X.-J.; Zhao, J.-S.; Jiang, J.-H.; Qian, J.-C.; Pang, D.H. Noble-metal-free CdS@MoS<sub>2</sub> core-shell nanoheterostructures for efficient and stabilized visible-light-driven H<sub>2</sub> generation. *Int. J. Hydrog. Energy* **2019**, *44*, 16657–16666. [[CrossRef](#)]
34. Tang, S.; Xia, Y.; Fan, J.; Cheng, B.; Yu, J.; Ho, W. Enhanced photocatalytic H<sub>2</sub> production performance of CdS hollow spheres using C and Pt as bi-cocatalysts. *Chin. J. Catal.* **2021**, *42*, 743–752. [[CrossRef](#)]
35. Maeda, K.; Terashima, H.; Kase, K.; Domen, K. Nanoparticulate precursor route to fine particles of TaON and ZrO<sub>2</sub>-TaON solid solution and their photocatalytic activity for hydrogen evolution under visible light. *Appl. Catal. A Gen.* **2009**, *357*, 206–212. [[CrossRef](#)]
36. Liu, Y.Y.; Zeng, C.M.; Ai, L.H.; Jiang, J. Boosting charge transfer and hydrogen evolution performance of CdS nanocrystals hybridized with MoS<sub>2</sub> nanosheets under visible light irradiation. *Appl. Surf. Sci.* **2019**, *484*, 692–700. [[CrossRef](#)]
37. Zubair, M.; Vanhaecke, E.M.M.; Svernum, I.H.; Ronning, M.; Yang, J. Core-shell particles of C-doped CdS and graphene: A noble metal-free approach for efficient photocatalytic H<sub>2</sub> generation. *Green Energy Environ.* **2020**, *5*, 461–472. [[CrossRef](#)]
38. Yang, G.W.; Chen, T.; Xing, C.W.; Tian, Z.C.; Hu, Y.J.; Yu, G.Y.; Li, X.Y. Construction of multi-scale 1D/2D CdS/ZnS(en)(0.5) nanorod/nanosheet heterojunction to boost photocatalytic hydrogen generation performance. *Appl. Surf. Sci.* **2022**, *578*, 152033. [[CrossRef](#)]
39. Wang, J.H.; Zhu, Q.; Liao, Y.W.; Fu, H.Q.; Chang, J.M.; Zhang, Y.L.; Kan, T.T.; Gao, H.J.; Huang, W.C. Efficient enhancement of photocatalytic hydrogen evolution of CdS nanorods by Nano-CuO. *J. Alloy. Compd.* **2021**, *883*, 160832. [[CrossRef](#)]
40. Zhang, J.; Qiao, S.Z.; Qi, L.F.; Yu, J.G. Fabrication of NiS modified CdS nanorod p-n junction photocatalysts with enhanced visible-light photocatalytic H<sub>2</sub> production activity. *Phys. Chem. Chem. Phys.* **2013**, *15*, 12088–12094. [[CrossRef](#)]
41. Sun, H.; Chen, J.; Liu, S.; Agrawal, D.K.; Zhao, Y.; Wang, D.; Mao, Z. Photocatalytic H<sub>2</sub> evolution of porous silicon derived from magnesiothermic reduction of mesoporous SiO<sub>2</sub>. *Int. J. Hydrog. Energy* **2019**, *44*, 7216–7221. [[CrossRef](#)]
42. Wang, W.; Fang, J. Mesoporous SiO<sub>2</sub>-derived g-C<sub>3</sub>N<sub>4</sub>@CdS core-shell heteronanostructure for efficient and stable photocatalytic H<sub>2</sub> production. *Ceram. Int.* **2020**, *46*, 2384–2391. [[CrossRef](#)]
43. Wang, X.J.; Tian, X.; Sun, Y.J.; Zhu, J.Y.; Li, F.T.; Mu, H.Y.; Zhao, J. Enhanced Schottky effect of a 2D-2D CoP/g-C<sub>3</sub>N<sub>4</sub> interface for boosting photocatalytic H<sub>2</sub> evolution. *Nanoscale* **2018**, *10*, 12315–12321. [[CrossRef](#)] [[PubMed](#)]